

Self-organization of linear nanochannel networks

R. K. Annabattula,¹ J. M. Veenstra,¹ Y. F. Mei,² O. G. Schmidt,² and P. R. Onck^{1,*}

¹Zernike Institute for Advanced Materials, University of Groningen, Nijenborgh 4, 9747 AG Groningen, The Netherlands

²Institute for Integrative Nanosciences, IFW-Dresden, Helmholtzstrasse 20, 01069 Dresden, Germany

(Received 4 January 2010; revised manuscript received 25 May 2010; published 24 June 2010)

A theoretical study has been conducted to explore the mechanics of self-organizing channel networks with dimensions in the submicron range and nanorange. The channels form by the partial release and bond back of prestressed thin films. In the release phase, the film spontaneously buckles into wrinkles of a certain wavelength, followed by a bond-back phase in which the final channel geometry is established through cohesive interface attractions. Results are presented in terms of the channel spacing, height, and width as a function of the film stiffness, thickness, eigenstrain, etch width, and interface energy. We have identified two dimensionless parameters that fully quantify the network assembly, showing excellent agreement with experiments. Our results provide valuable insight for the design of submicron and nanoscale channel networks with specific geometries.

DOI: 10.1103/PhysRevB.81.224114

PACS number(s): 68.60.Bs, 68.55.J–

I. INTRODUCTION

Microchannels and nanochannels play an important role as liquid handling systems in present-day microdevices and nanodevices. They have been successfully used for many technological applications such as DNA manipulation,^{1,2} microfluidic transport in microreactors³ and micromixers.⁴ The continuous miniaturization of microsystems and the associated reduction in channel dimensions can have great implications for biochemical research as it can lead to a considerable reduction in analysis time,⁵ reduction in sample size⁶ and it opens up the possibility to perform analyses in parallel on a single chip allowing high throughput.⁷ Therefore, the fabrication of submicrometer/nanometer sized channels with controllable dimensions has gained considerable interest in recent years. Various methods to fabricate such channel networks have appeared and almost all of them are based on the three-step process of conventional lithography, thin film deposition, and etching.^{8–12}

An alternative approach that has been successfully explored is based on the self-organization of surface patterns and channels through the buckling of prestressed thin films. Thin-film buckling has been explored in a wide range of applications in the last decade^{13–19} and offers the advantage that the surface does not need to be prepatterned and thus eliminates the expensive and time-consuming lithographic steps. Instead, the buckling-driven self-organization relies on a spontaneous buckling process that allows surface micropatterns (wrinkles, channels) to be formed that have a periodicity much smaller than the macroscopically induced features. The ability to fabricate ordered submicron or nanochannel networks by the controlled wrinkling/buckling of thin films can possibly push forward the still evolving field of microfluidic large-scale integration,²⁰ similar to the large-scale integration in microelectronics. Self-organized buckles can be generated by depositing stiff thin films on expanded (by heating or stretching) compliant substrates.^{21–23} The key mechanism in this method is the generation of anisotropy in the prebuckling or postbuckling stress state, allowing one preferred direction to be identified in which the buckles line

up. This directionality can also be introduced by the controlled release of the bonding between film and substrate using chemical underetching (e.g., Mei *et al.*,²⁴ Malachias *et al.*²⁵) or electrolysis (e.g., Edmondson *et al.*²⁶). Then, the film first buckles up from the substrate when released, relaxing its stresses, followed by bond back to the substrate due to cohesive film/substrate forces, freezing in the final channel geometry. The aim of the current paper is to explore the relation between the final channel geometry and the system parameters for this release-and-bond-back approach. To do so, we will focus on the experimental setup as presented by Mei *et al.*²⁴ A similar effect of cohesive van der Waals forces can result in the spontaneous formation of surface wrinkles in film/substrate systems separated by a fluid layer.²⁷

In the work of Mei *et al.*,²⁴ a thin film of $\text{Si}_{0.76}\text{Ge}_{0.24}$ is epitaxially grown on a sacrificial layer (SiO_2) on a Si substrate [see Fig. 1(a)]. The thickness of the film and sacrificial

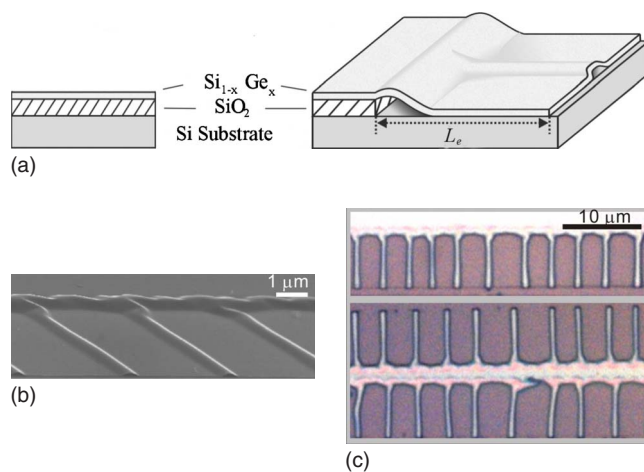


FIG. 1. (Color online) (a) Nanochannel fabrication procedure of Mei *et al.* (Ref. 24) in which a thin SiGe film is grown on a SiO_2 sacrificial layer located on a Si substrate. (b) SEM image of a single-sided channel network and (c) optical micrographs of a single-sided (top) and a double-sided (bottom) branch network. Reproduced with permission from Mei *et al.* (Ref. 24).

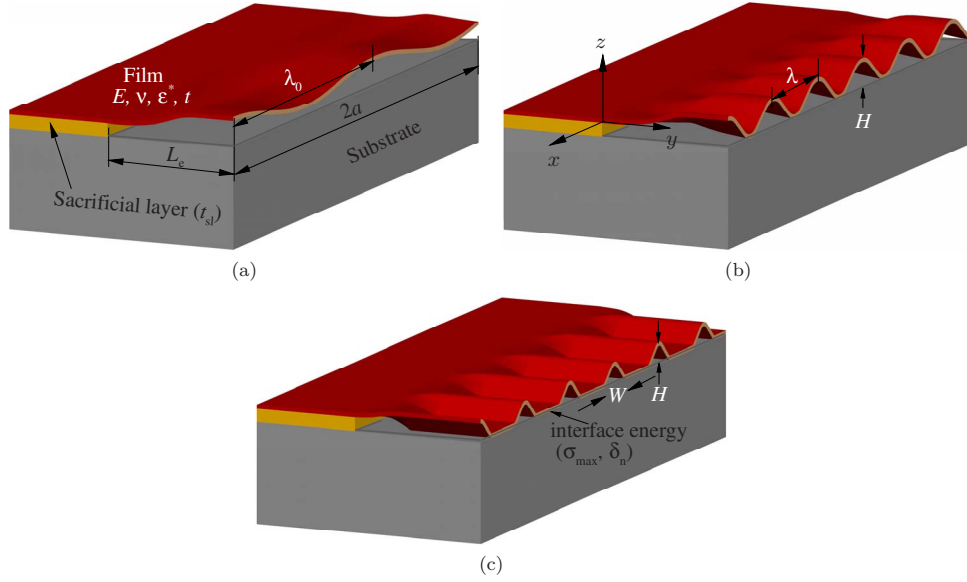


FIG. 2. (Color online) Schematic of the process of channel formation. (a) Initial buckling of the film. (b) Configuration of the film at the end of eigenstrain loading. (c) Configuration showing the channels after bond back of the film to the substrate.

layer are 20 nm and 100 nm, respectively. An etching solution of hydrofluoric acid is used to etch the sacrificial layer from one side [from the right in Fig. 1(a)] so that the film can release its eigenstrains (induced during the epitaxial growth process due to lattice mismatch between the film and the substrate) by buckling with a specific wavelength. After the etching process is stopped, the system is left for drying, during which the film bonds back to the substrate due to the cohesive attraction between the film and the substrate. Figure 1(b) shows a SEM image of a single branch channel network and Fig. 1(c) shows optical micrographs of a double- and single-branch submicron channel network.²⁴ The objective of this paper is to understand the mechanics underlying the self-organized channel formation. To do so, we will develop a computational model to describe the evolution of the spacing, width, and height of the channels formed as a function of the system parameters, such as the film width, thickness, elastic modulus, and eigenstrain, and the film/substrate interface energy.

The paper is organized as follows. In Sec. II, we will describe the boundary value problem representing the thin-film setup and discuss the theoretical and numerical mechanical models used to solve it. In Sec. III, the results are presented; we will subsequently analyze the onset of buckling (Sec. III A), the postbuckling stage as a function of eigenstrain (Sec. III B) and, finally, in Sec. III C, bonding back. Then, we will compare the modeling results with the experiments and complete the discussion with conclusions in Sec. IV.

II. PROBLEM DEFINITION AND METHOD

In this section, we develop a model to describe the experimental process shown in Fig. 1. There are three important stages in the process of channel formation: (i) film growth, during which the film is prestrained (with an eigenstrain ϵ^*)

due to lattice mismatch between the film and the substrate, (ii) buckling of the film into wrinkles with a characteristic periodicity, channel height, and width due to removal of the sacrificial layer and (iii) bond back of the film to the substrate due to cohesive attraction during drying. In this process, the sacrificial layer is progressively removed so that the etch width L_e [see Fig. 1(a)] increases in time. In our model, however, we will study the effect of L_e on the buckling behavior by fixing L_e and progressively increasing ϵ^* . By doing so, we implicitly assume that dissipation mechanisms are absent in the film/substrate system.

With the above assumptions, the stages (i) and (ii) can be combined, yielding a two-step process consisting of an eigenstrain loading step followed by bond back as shown in Fig. 2. We study a long film of length $2a$, width L_e , and thickness t , separated by a distance t_{sl} (the thickness of the sacrificial layer) from the substrate. The film is fully constrained along one longitudinal edge, where the sacrificial layer is still present, and free at the other three edges. The film in this configuration is loaded quasistatically by an eigenstrain (from $\epsilon^*=0$ to 1.1%), during which it will go through three consecutive stages. First, the film will buckle with a characteristic wavelength λ_0 at a critical buckling strain ϵ_c^* , that is much smaller than the total eigenstrain in the film [see Fig. 2(a)]. To calculate the critical strain ϵ_c^* and wavelength λ_0 , we will perform a buckling analysis in Sec. III A. With further increase in eigenstrain, the film enters into a postbuckling regime, during which the wavelength decreases from λ_0 to λ and the buckling amplitude increases from approximately zero to H as shown in Fig. 2(b). This will be the topic of Sec. III B. When all strain has been released the sample is left to dry during which the film bonds back to the substrate. This is implemented by increasing the interface energy between the film and the substrate, based on a cohesive interface law.²⁸ During bond back, we will only consider normal tractions to be present so that the interface energy only depends on σ_{\max} , the maximum traction, and δ_n ,

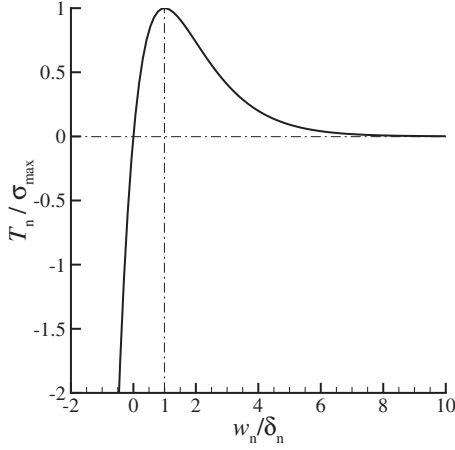


FIG. 3. Cohesive traction-separation law between the film and the substrate. The normal traction T_n is normalized by σ_{\max} and the normal opening w_n by δ_n .

the critical opening (see Fig. 3). As a result of the film/substrate attraction, the channel width and height gradually reduce, reaching a final channel configuration as shown in Fig. 2(c). This will be the subject of Sec. III C.

Using von Karman nonlinear plate theory, the total strain in the film can be written as the sum of three contributions,²⁹

$$\boldsymbol{\varepsilon} = \boldsymbol{\varepsilon}^{\text{str}} + \boldsymbol{\varepsilon}^{\text{rot}} + \boldsymbol{\varepsilon}^{\text{bend}}.$$

The first term, $\boldsymbol{\varepsilon}^{\text{str}}$, is the strain caused by the in-plane stretching of the material and its coefficients with respect to a Cartesian frame in the x - y plane [see Fig. 2(b)] are

$$\varepsilon_{ij}^{\text{str}} = \frac{1}{2} \left(\frac{\partial u_i}{\partial x_j} + \frac{\partial u_j}{\partial x_i} \right), \quad i = 1, 2, \quad j = 1, 2 \quad (1)$$

with u_i the in-plane displacements. The second term, $\boldsymbol{\varepsilon}^{\text{rot}}$, is the contribution caused by the out-of-plane displacements w and is given by

$$\varepsilon_{ij}^{\text{rot}} = \frac{1}{2} \frac{\partial w}{\partial x_i} \frac{\partial w}{\partial x_j}, \quad i = 1, 2, \quad j = 1, 2. \quad (2)$$

The contribution of the strain caused by bending/curvature of the plate is given by

$$\varepsilon_{ij}^{\text{bend}} = -z \frac{\partial^2 w}{\partial x_i \partial x_j} = -z \chi_{ij}, \quad i = 1, 2, \quad j = 1, 2. \quad (3)$$

For the constitutive behavior of the film, we assume that the total strain consists of an elastic part $\boldsymbol{\varepsilon}^{\text{el}}$ and an eigenstrain part $\boldsymbol{\varepsilon}^{\text{eig}}$: $\boldsymbol{\varepsilon} = \boldsymbol{\varepsilon}^{\text{el}} + \boldsymbol{\varepsilon}^{\text{eig}}$, with the eigenstrain given by

$$\varepsilon_{ij}^{\text{eig}} = \varepsilon^* \delta_{ij}, \quad i = 1, 2, \quad j = 1, 2 \quad (4)$$

with δ_{ij} the Kronecker delta. The film is in a state of plane stress ($\sigma_{13} = \sigma_{23} = \sigma_{33} = 0$) so that the coefficients of the stress $\boldsymbol{\sigma}$ in the plate are given by

$$\sigma_{ij} = \frac{E}{1 + \nu} \left(\varepsilon_{ij}^{\text{el}} + \frac{\nu}{1 - \nu} \varepsilon_{kk}^{\text{el}} \delta_{ij} \right), \quad (5)$$

where $i = 1, 2, j = 1, 2$, E is Young's modulus, and ν is Poisson's ratio of the film. To mimic the complex interplay be-

tween the film and substrate during drying, we assume a phenomenological interaction relation that consists of a short-range repulsive part and a long-range attractive part (see Fig. 3), also often employed for van der Waals-type interactions. During bond back, the film experiences a vertical downward traction T_n , causing the normal separation w_n between the film and substrate to decrease. For this, we use a nonlinear traction-separation relation given by Xu and Needleman,²⁸

$$T_n = \sigma_{\max} \frac{w_n}{\delta_n} \exp \left(1 - \frac{w_n}{\delta_n} \right), \quad (6)$$

where σ_{\max} is the maximum normal traction attained at the critical normal opening δ_n (see Fig. 3). The cohesive energy per unit area is equal to $\Gamma = \int_{w_n} T_n dw_n = \sigma_{\max} \delta_n \exp(1)$.

To investigate which dimensionless parameters govern the deformation of the film during the eigenstrain loading step, we will carry out a dimensional analysis based on the principle of virtual work. From the dimensional analysis (see the Ref. 30, Sec. I), it follows that for plates with the same ν , a/L_e and similar boundary conditions, the solution only depends on the unique factor $\varepsilon^* a L_e / t^2$, independent of the stiffness. For the boundary value problem of interest, the length of the plate is much larger than its width so that $L_e/a \rightarrow 0$. From the above condition it follows that the solution only depends on the governing dimensionless number $\varepsilon^* (L_e^2/t^2)(1 + \nu)$.

III. RESULTS AND DISCUSSION

In this section, we present the results of the evolution of buckling wavelength (λ), buckling height (H), and channel width (W) for the boundary value problem shown in Fig. 2. First, in Sec. III A we derive an analytical solution for the critical buckling strain and buckling wavelength for the boundary value problem at the initiation of buckling. Then in Sec. III B, we use the finite-element method to numerically study the evolution of wavelength and buckling height of a free-standing thin film, neglecting any interaction with the substrate. Finally, in Sec. III C we perform bond-back simulations to obtain the final dimensions (in terms of H , W , and λ) of the channels and compare the results with the experimental data.

A. Buckling analysis

The thickness t of the film (≈ 20 nm) is much smaller than the length $2a$ (≈ 100 μm) and etching width L_e ($\approx 2-6$ μm) (see Fig. 2). Hence, the film can be modeled as a thin plate based on von Karman nonlinear plate theory. The Si-Ge film material is assumed to be isotropic and linear elastic. For such a free-standing film under a uniform in-plane stress state, it can be shown (see the Ref. 30, Sec. II for complete derivation) that the critical buckling coefficient is given by $K = 1.28$ and the critical buckling stress σ_c (or critical eigenstrain ε_c^*),

$$\frac{\sigma_c}{E} = \varepsilon_c^* = \frac{1.28 \pi^2}{12(1 - \nu^2)} \left(\frac{t}{L_e} \right)^2 \quad (7)$$

with a wavelength

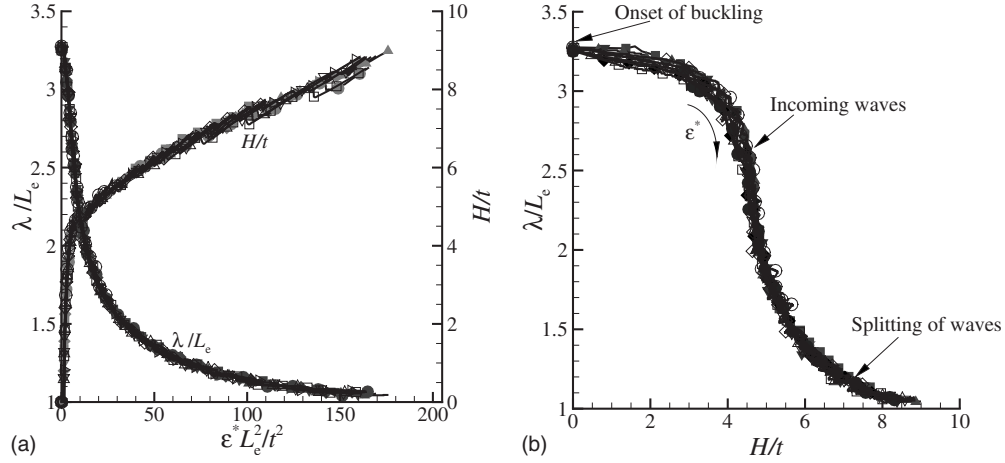


FIG. 4. (a) Normalized wavelength (λ/L_e) and normalized channel height (H/t) versus normalized strain. (b) Normalized wavelength versus normalized channel height. The plots (a) and (b) contain the results for $1 \leq L_e \leq 6 \mu\text{m}$ and $t = 10$ and 20 nm .

$$\lambda_0 = \frac{L_e}{0.3} \approx 3.3L_e. \quad (8)$$

B. Postbuckling analysis

The postbuckling response of the film due to eigenstrain loading will be simulated using the finite-element method.³¹ The simulations are performed using a film of length $2a = 100 \mu\text{m}$, with an etch width in the range of $1 \leq L_e \leq 6 \mu\text{m}$ (steps of $1 \mu\text{m}$) for two different thicknesses t (10 and 20 nm). The elastic modulus E of the film ($\text{Si}_{0.76}\text{Ge}_{0.24}$) is 120 GPa and Poisson's ratio ν is 0.32. We model half the length of the film and apply symmetry boundary conditions at $x = -a$ [see Fig. 2(b)]. Furthermore, we kinematically constrain the edge connected to the sacrificial layer ($y = 0$) and leave the other edges ($x = 0$ and $y = L_e$) stress free. The film is discretized using four-noded shell elements (S4) with full integration and the substrate is modeled as a rigid surface. Geometric nonlinearity is incorporated in the model to account for large rotations. To trigger buckling the initial configuration of the film is perturbed in the out-of-plane direction (z direction) with sufficiently small imperfections. An element size of $0.1 \mu\text{m}$ is found to be small enough for mesh convergence for all etch widths. The eigenstrain ϵ^* is incrementally increased to 1.1%, taking very small increments initially so that the critical buckling strain ϵ_c^* can be accurately determined. (The critical buckling strain is taken to be the eigenstrain at which the uniform in-plane stress state suddenly relaxes and the film starts to deflect laterally.) The (buckling) wavelength reported in the simulations is measured at the free longitudinal edge [see Fig. 2(b)]. For each value of L_e , we have compared the initial buckling strain ϵ_c^* and wavelength λ_0 with Eqs. (7) and (8), showing excellent agreement.

Figure 4(a) shows the evolution of the normalized wavelength λ/L_e and amplitude H/t [see Fig. 2(b)] as a function of the dimensionless straining quantity $\epsilon^* L_e^2/t^2$, as derived in Sec. II. The wavelength and amplitude reported are measured at the free longitudinal edge of the film corresponding to the

highlighted face in Fig. 2. Figure 4(a) shows that the initiation of buckling (at small strains ϵ^*) occurs at a wavelength $\lambda_0 = 3.3L_e$ [conform Eq. (8)]. For a given L_e and t , the wavelength first decreases rapidly with strain, after which it saturates at $\lambda \approx L_e$. Figure 4(a) also shows that for given film dimensions, the height of the buckles first increases rapidly with strain, after which it changes to a more moderate rate of increase at $H \approx 4.5t$. For a given strain and thickness, both the wavelength λ and buckle height H increase with L_e indicating that a film of small width L_e accommodates a given eigenstrain by buckling into many buckles of small amplitude while for a larger film width, the film's strain energy is minimized for a lower number of buckles but with a higher amplitude. In addition, comparison of the results for the different thicknesses shows that both wavelength and amplitude increase with thickness, for a given L_e and ϵ^* . The trends shown in of Fig. 4(a) are in close agreement with the analytical results of Fedorchenko *et al.*,¹⁸ who used minimization of the free energy in the film, assuming an infinitely long film with a purely sinusoidal wave in the longitudinal direction.

It turns out that the system uses two different mechanisms to accommodate the internal straining. The first is operative at small strains and proceeds through the entering of new buckles from the free edge [see Fig. 5(a)]. As can be observed from Fig. 5(a), the system can accommodate the strain by increasing the number of buckles at a more-or-less constant amplitude. At the moment, the wavelength reaches a critical value, the energy cost of allowing new buckles increases sharply and a second mechanism becomes operative. At this stage of constant wavelength, straining the film develops a narrow strip of large compressive membrane stress adjacent to the constrained edge of the film. The width of the strip decreases and the compressive stress intensity increases as ϵ^* increases. Thus for sufficiently large ϵ^* , the strip may buckle into wrinkles³² as can also be seen in Fig. 5(c) and in Fig. 2(c) of Mei *et al.*²⁴ The wrinkles initiate the process of splitting of buckles [see Fig. 5(b)], the second mechanism of strain accommodation. This phenomenon of sudden change in wavelength in the postbuckling regime has been referred to as “mode-jumping”³³ in the literature.^{34,35}

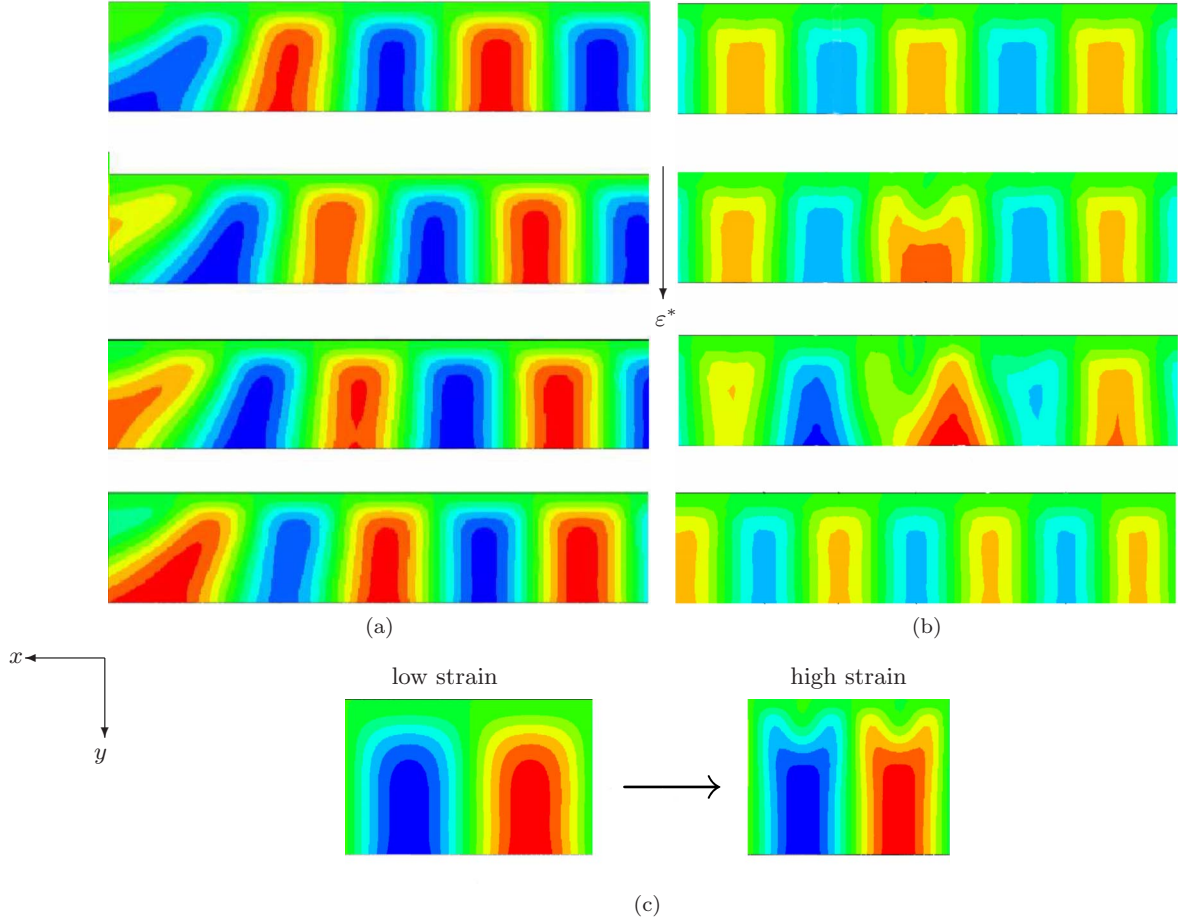


FIG. 5. (Color online) Two different mechanisms of strain accommodation in the film. (a) Waves entering from the free edge (left) with increasing eigenstrain. Note that only a portion of the film from the free edge is shown. (b) Process of splitting of buckles with further increase in eigenstrain. (c) Configurations at low and high eigenstrains depicting the initiation of splitting of buckles at the fixed edge. The colors indicate the deflections w in the z direction with red (contours with enhanced white boundary in monochrome) being positive and blue (contours with less pronounced white boundary in monochrome) being negative. The eigenstrain increases from snapshot to snapshot in the downward direction.

The results for H and λ in Fig. 4(a) can now be combined to show the evolution of wavelength versus amplitude [Fig. 4(b)], which can be directly related to the strain accommodation mechanisms. In the initial stages of buckling, the film accommodates the strain by increasing its buckling amplitude while keeping the wavelength almost constant. Then, new waves start entering the system, which reduces the system's wavelength considerably at almost constant buckling amplitude. Once the number of incoming waves from the free edge saturates, the amplitude increases again until the other mode of strain accommodation becomes operative, resulting in splitting of buckles. The simulation results show a unique relation between the square of the height/wavelength ratio and eigenstrain, $(H/\lambda)^2 = 0.45\epsilon^*$, independent of the film dimensions t and L_c (results not shown).

This proportionality of $(H/\lambda)^2$ with ϵ^* is a direct consequence of the fact that the wavelength and amplitude must satisfy the constraint that the total contour length of the film is dictated by the eigenstrain released. This dependence can be rationalized by writing the profile of the film along the free edge in the x - z plane [film-shape variations in the y direction, see Fig. 2(b)] as

$$w(x) = H \sin(2\pi x/\lambda) \quad (9)$$

with H the buckling amplitude and λ the wavelength. The contour length of the film for one wavelength is given by

$$l_c = \int_0^\lambda \sqrt{1 + \left(\frac{dw}{dx}\right)^2} dx \approx \lambda + \frac{\pi^2 H^2}{\lambda}, \quad (10)$$

assuming the slope dw/dx of the profile to be small. The eigenstrain in the film is related to the contour length according to $\epsilon^* = (l_c - \lambda)/\lambda$, which yields

$$\epsilon^* \approx \frac{H^2 \pi^2}{\lambda^2}. \quad (11)$$

The results discussed so far neglect any cohesive interaction between the film and the substrate. However, for the situations where such an interaction is present, the buckling profile will change at the moment the film and substrate touch at the free edge. To explore how this instance of touch-down depends on the system parameters, we use the dimensionless results for H/t of Fig. 4(a). By equating $H/2$ to t_{sl} ($=100$ nm), we can find the etch width L_e at touchdown for

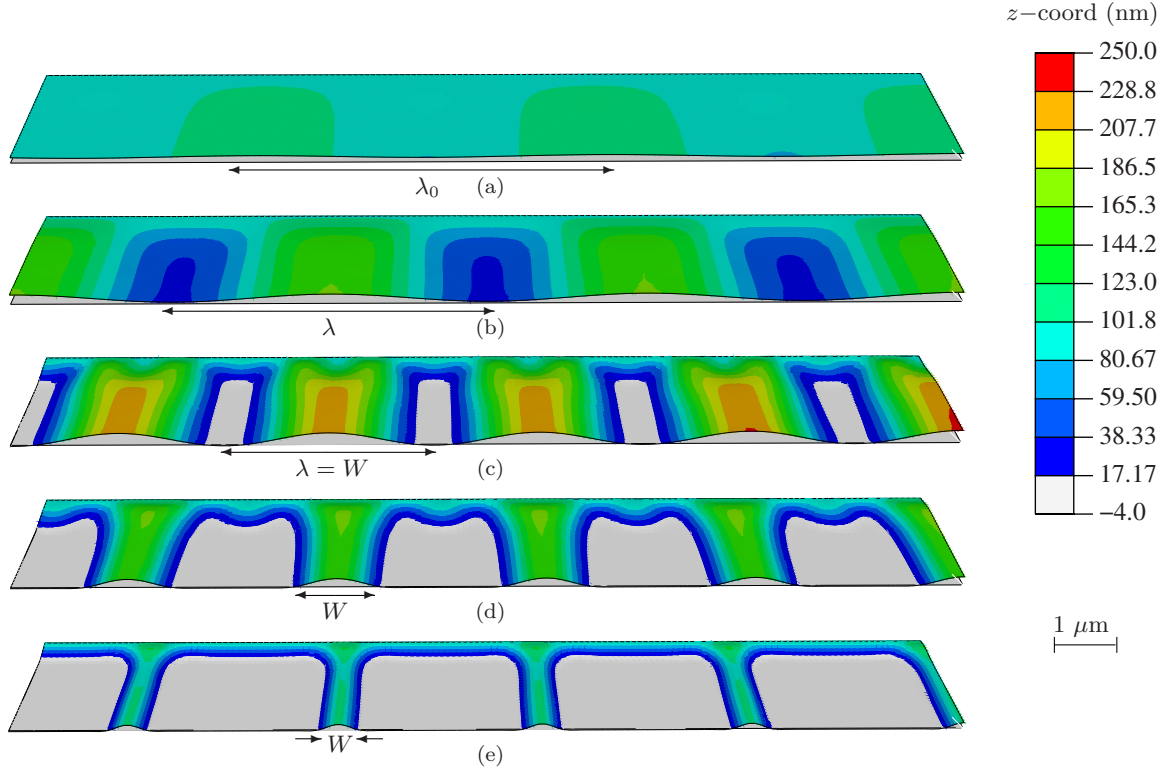


FIG. 6. (Color online) Configurations of the film at various instances of channel formation for $L_e = 3 \mu\text{m}$, $t = 20 \text{ nm}$, and $\varepsilon^* = 1.1\%$. Only a portion of the film from the symmetric edge (located at the right) is shown. The corresponding simulation times are (a) $2.46 \mu\text{s}$, (b) $27 \mu\text{s}$, (c) $82 \mu\text{s}$, (d) $98.33 \mu\text{s}$, and (e) $282 \mu\text{s}$.

a given t_{sl} , ε^* , and t . In the experiments of Mei *et al.*,²⁴ the thickness of the sacrificial layer is 100 nm , the thickness of the film is 20 nm , and the eigenstrain is 1.1% , resulting in an L_e at touchdown $\approx 2.5 \mu\text{m}$. As the interaction between the film and the substrate is weak, it is not expected that the event of touchdown in the Si-Ge system will affect the final channel morphology. Indeed, this is the case since long and regular channels can be formed, much longer than the calculated $2.5 \mu\text{m}$. However, it was shown that in the situation of an $\text{In}_{0.2}\text{Ga}_{0.8}\text{As}$ film on a AlAs substrate system, the touchdown of the film changes the channel morphology²⁵ due to the strong interaction between the film and the substrate during the buckling-up stage itself. In this system, the eigenstrain is 1.4% , the thickness of the sacrificial layer is 80 nm , and the film thickness is 20 nm , yielding an etch width at touchdown $\approx 2.0 \mu\text{m}$, in very close agreement with the observations in the experiments (see Fig. 3 of Malachias *et al.*²⁵). This nicely exemplifies how the dimensionless results of Fig. 4 can be used to tune the instance of touchdown for experimental film systems.

C. Bond back

The bond back of the film starts when the film has completely released its eigenstrains and the system is left for drying. To overcome the local instabilities triggered by the simultaneous occurrence of multiple splitting events during eigenstrain loading, we resort to a fully dynamic solution procedure to simulate the entire buckling-up and bond-back

process. In the dynamic solution procedure, we use a mass-proportional damping and choose the eigenstrain loading rate to be sufficiently low, mimicking a quasistatic procedure in order to minimize the kinetic energy in the system. The results of the static and dynamic procedure were compared for small etch widths (for which no multiple splitting occurred) and the results were found to coincide. Once the eigenstrain loading step has completed, the cohesive forces between the film and the substrate are increased to bond back the film on the substrate. This process has been incorporated by increasing the interface strength σ_{max} in time while keeping δ_n constant according to the Xu-Needleman cohesive relation shown in Eq. (6) and Fig. 3. Once the film nodes touch the substrate, they are effectively anchored at that location from that instant onward.

Figure 6 shows five configurations during the process of channel formation from the initiation of buckling through buckling up and bonding back for a film of width $L_e = 3 \mu\text{m}$ and thickness 20 nm . In Fig. 6(a), the eigenstrain reaches the critical buckling strain ε_c^* , causing the film to buckle with the buckling wavelength $\lambda_0 = 3.3L_e$. Then, with increasing eigenstrain, the wavelength λ decreases and the amplitude increases [Fig. 6(b)], until all the strain has been applied and the wavelength is minimal while the amplitude is maximal [Fig. 6(c)]. Then, the interface energy is enhanced (taking $\delta_n = 10 \text{ nm}$ and increasing σ_{max}) and the film starts bonding back [Fig. 6(d)], during which the wavelength λ stays constant but the channel width W and height H decrease until the final channel configuration has been reached [Fig. 6(e)]. Figure 7 shows the corresponding evolution of

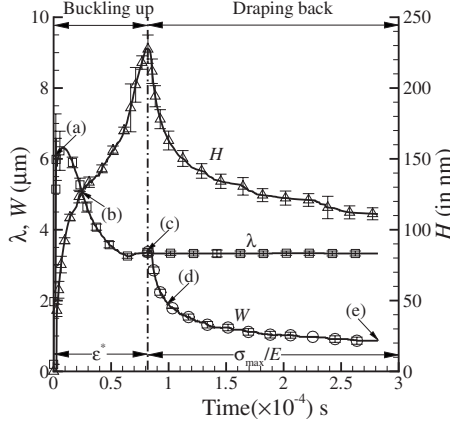


FIG. 7. Evolution of wavelength λ , channel width W , and channel height H as a function of time. The buckling-up and bond-back stages are shown for each curve. The loading parameter during the buckling-up stage is the eigenstrain (ε^*) and during the bond-back stage is the interface strength (σ_{\max}). The ε^* reaches a maximum value of 1.1% at the end of the buckling-up stage (i.e., at time = 82 μ s). The normalized loading parameter (σ_{\max}/E) is increased from zero (at time = 82 μ s) to 1.67×10^{-4} at the end of the bond-back step. The film dimensions are $L_e = 3 \mu\text{m}$ and $t = 20 \text{ nm}$, respectively. The labels (a)–(e) corresponds to Figs. 6(a)–6(e).

wavelength (λ), channel width (W), and channel height (H) as a function of time. The loading parameter during the buckling-up stage is the eigenstrain and during the bond-back stage is the cohesive attraction. The eigenstrain loading process takes 82 μ s during which the strain is increased to 1.1%. Then, the bond-back process starts (with $\Gamma = \sigma_{\max} = 0$) and continues for 200 μ s until $\sigma_{\max}/E = 1.67 \times 10^{-4}$ (or $\Gamma = 0.2 \text{ J/m}^2$). The two processes are distinguished by a vertical line in the figure. The error bars in Fig. 7 corresponds to the standard deviation of the measured quantities, indicating that the fluctuations are large compared to the static results (Fig. 4) but still small compared to the average. There are oscillations due to inertia at small strains, particularly at the onset of buckling. However, as the eigenstrain reaches 1.1%, the kinetic energy reduces to zero and the system reaches a steady-state behavior. In all the simulations during the bond-back step, the wavelength λ remains unchanged and the channel height H and channel width W progressively reduce, gradually converging to a saturation point. Note that the results of Fig. 7 have been obtained for a fixed value of δ_n . We have repeated the simulations for different values of δ_n and found that the dependence on δ_n is negligibly small compared to Γ (i.e., keeping Γ fixed by doubling δ_n and halving the σ_{\max} did not affect the results shown in Fig. 7). This shows that the interface response is dominated by the energy per unit area Γ and not by the individual components σ_{\max} and δ_n .

During bond back, the wavelength λ does not change anymore and this becomes a characteristic length scale in this phase. The ensuing width and height depend on the balance between the interface energy in the rebonded region, λ - W , and the strain energy in the film.²⁶ By only accounting for bending in the x - z plane and neglecting the stretching energy, this energy balance can be written as

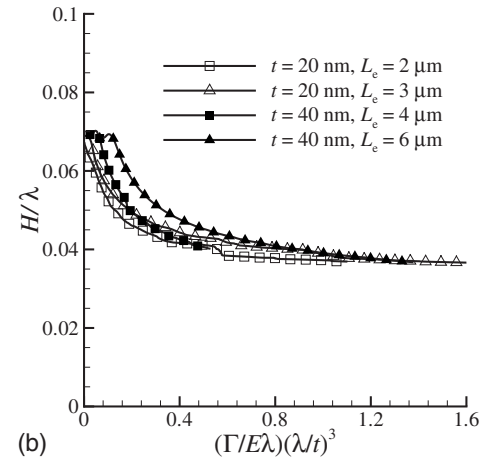
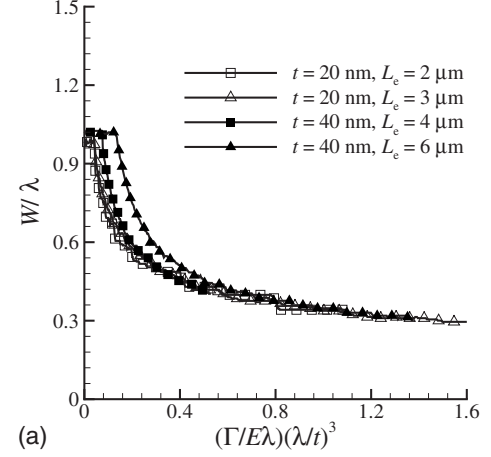


FIG. 8. Evolution of the normalized (a) channel width W/λ and (b) channel height H/λ during the bond-back process.

$$\frac{Et^3 L_e}{12(1-\nu^2)} \int_0^\lambda \left(\frac{d^2 w}{dx^2} \right)^2 dx = \Gamma(\lambda - W)L_e \quad (12)$$

with w the vertical deflection and Γ the interface energy per unit area. By normalizing all lengths with λ in Eq. (12), i.e., $w = \bar{w}\lambda$ and $x = \bar{x}\lambda$, it follows that

$$\frac{Et^3}{12(1-\nu^2)\lambda} \Phi_b = \Gamma(\lambda - W) \quad (13)$$

with Φ_b the dimensionless bending energy defined as

$$\Phi_b = \int_0^1 \left(\frac{d^2 \bar{w}}{d\bar{x}^2} \right)^2 d\bar{x}. \quad (14)$$

The height H for a given λ depends on the current eigenstrain ε^* [see Eq. (11)] and therefore enters the dimensionless bending energy Φ_b . By dividing Eq. (13) by λ^2 and rearranging it can be deduced that W/λ (and H/λ) depend solely on the dimensionless number $(\Gamma/E\lambda)(\lambda/t)^3$ and eigenstrain ε^* . Figure 8 shows this dependence for the simulation results similar to Fig. 7 for $\varepsilon^* = 1.1\%$ and different values of L_e and t , collapsing all data on one universal bond-back curve. This curve could assist in backing out the cohesive

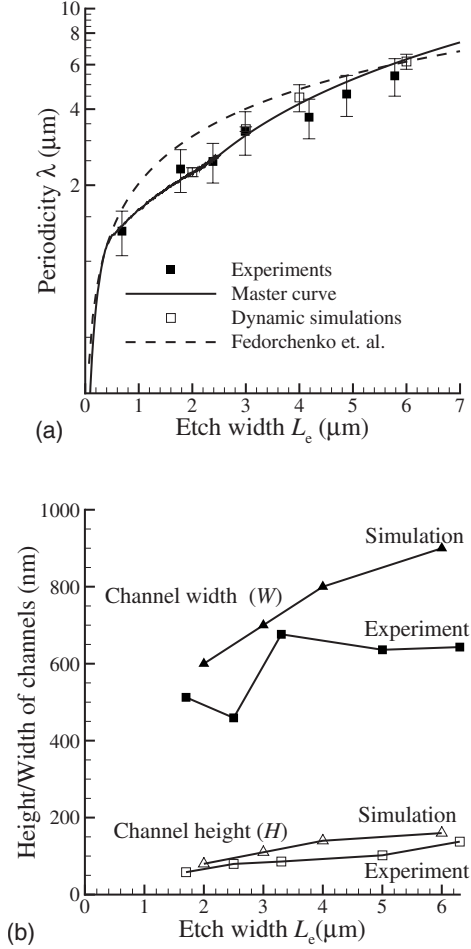


FIG. 9. (a) Comparison of periodicity of buckles/channels with the experiments ($t=20$ nm). The results are also compared with the analytical solution of Fedorchenko *et al.* (Ref. 18). The results for the static simulation for $L_e > 3$ μm is obtained by extrapolating the master curve [Fig. 4(a)] beyond $\varepsilon^*(L_e/t)^2 > 165$ with $\lambda/L_e = 1.1$. (b) Comparison of final channel height and width of the simulations with the experiments. The simulation results are shown by triangles, whereas experiments are shown by square symbols. The results for the experiment and simulations are shown for a film of thickness 20 nm.

interface energy Γ for experimental film/substrate systems of which the film properties and eigenstrain are known. Once this energy has been determined, the results of Fig. 8 can be used to design the experimental parameters for a target channel morphology.

Next, we compare the results obtained from the simulations with the experimental data reported by Mei and co-workers.²⁴ Figure 9(a) shows the predictions for the wavelength from the master curve of Fig. 4(a) for an eigenstrain of 1.1% and a thickness $t=20$ nm, where we have extrapolated the master relation by taking $\lambda/L_e = 1.1$ for $\varepsilon^*(L_e/t)^2 > 165$. The prediction of the wavelength extracted from the master curve and the dynamic simulations (Fig. 7) match very well with the experimental results. We have also plotted the analytical results of Fedorchenko *et al.*¹⁸ in Fig. 9(a) (dashed-dotted line) which show good agreement with both the simulations and experiments, especially at small L_e .

The wavelength results in Fig. 9(a) can be summarized as a bilinear relation having a slope of 3.3 at small L_e and a slope of 1.1 at large L_e . This clearly indicates that for the experimental strains of 1.1%, the wavelength at small L_e is determined by the initiation of buckling [see Eq. (8) and Fig. 4(a) at small $\varepsilon^*(L_e/t)^2$], after which it transforms to the limit of $\lambda/L_e = 1.1$ at large $\varepsilon^*(L_e/t)^2$ (see Fig. 4). Note, however, that the simulation results slightly overestimate the experimentally measured wavelengths for large etch widths L_e [see Fig. 9(a)].

In Fig. 9(b), we plot the final channel configuration W and H at the end of the dynamic simulations (as, for instance, depicted in Fig. 7) and compare them with the experimental data points. The correspondence is good, although the experimental values are slightly overestimated. It should be noted that the cohesive parameters in Eq. (6) and Fig. 3, are the free parameters in the model—no independent experimental data are available for the system under consideration. However, comparing our simulations with the experiments can give a first order estimation of the interface energy of the experimental system. The numerical data plotted in Fig. 9(b) correspond to $\Gamma = 0.2$ J/m². Since E and t are known and λ is predicted with good accuracy, the reasonable agreement of the simulations with the experiments suggests that Γ is in the range 0.1–1 J/m² (the simulations slightly overestimate the experimental data so that a somewhat larger interface energy is needed to further reduce the channel dimensions).

IV. SUMMARY AND CONCLUSIONS

We have used analytical and numerical calculations to describe the self-organization of branched channel networks through the controlled release of prestressed thin films. During this process three different stages can be identified. (i) The process is initiated by film buckling into the lowest eigenmode having a wavelength λ equal to 3.3 times the etch width L_e [Eq. (8)]. (ii) Then, with further straining the system enters a postbuckling regime in which the wavelength gradually decreases to 1.1 times L_e [Fig. 4(a)]. At first, the system can accommodate the additional film strains by decreasing its wavelength by allowing new waves to enter at a more-or-less constant amplitude. However, when the wavelength becomes approximately equal to the etch width, this accommodation mechanism saturates. The wrinkle amplitude increases, stresses build up, causing the energy cost of allowing new waves to sharply increase. Then, the system switches to a second accommodation mechanism, consisting of the splitting of existing buckles [Figs. 4(b) and 5]. (iii) Once the eigenstrains have been released the film is allowed to bond back to the substrate through an enhanced cohesive attraction. During this stage the actual final channel geometry is established with a branch channel spacing equal to the final buckling wavelength λ of stage (ii) and a channel width and height that gradually decrease with the increasing interface energy (Figs. 6 and 8).

During stage (ii), the buckling amplitude increases until the film touches the substrate. Here, the thickness of the sacrificial layer enters the analysis and dictates the maximum etch width that can be reached before touchdown. This limits

the formation of straight channels for systems with a strong interaction between film and substrate. By comparing the theoretical results with experimental data, we were able to rationalize the (limited) straight-channel length for two different experimental film/substrate systems.^{24,25} We have also compared the final channel spacing, height, and width of the branched networks with experiments, showing good agreement.

For each stage, the characteristic dimensionless parameters have been identified that drive the process. In stage (i), the slenderness ratio t/L_e determines the eigenstrain needed to initiate buckling, representative of typical Euler buckling behavior. In stage (ii), the evolution of the wavelength is a

unique function of $\varepsilon^*(L_e/t)^2$ while during the bond-back phase i.e., stage (iii), the final channel dimensions are governed by the bond-back parameter $(\Gamma/E\lambda)(\lambda/t)^3$. These results cannot only be used to back out the cohesive interface energy for experimental film/substrate systems, they can also provide guidelines for the design of specific channel network geometries.

ACKNOWLEDGMENT

The authors would like to acknowledge the financial support from MicroNed, The Netherlands under the project *FUNMOD-WP-4-C-4*.

*p.r.onck@rug.nl

- ¹S. W. Turner, A. M. Perez, A. Lopez, and H. G. Craighead, *J. Vac. Sci. Technol. B* **16**, 3835 (1998).
- ²M. Foquet, J. Korlach, W. Zipfel, W. W. Webb, and H. G. Craighead, *Anal. Chem.* **74**, 1415 (2002).
- ³H. Löwe, V. Hessel, and A. Mueller, *Pure Appl. Chem.* **74**, 2271 (2002).
- ⁴C. K. L. Tan, M. C. Tracey, J. B. Davis, and I. D. Johnston, *J. Micromech. Microeng.* **15**, 1885 (2005).
- ⁵R. A. Mathies and X. C. Huang, *Nature (London)* **359**, 167 (1992).
- ⁶A. T. Woolley and R. A. Mathies, *Proc. Natl. Acad. Sci. U.S.A.* **91**, 11348 (1994).
- ⁷M. Elwenspoek, T. S. J. Lammerink, R. Miyake, and J. H. J. Fluitman, *J. Micromech. Microeng.* **4**, 227 (1994).
- ⁸M. B. Stern, M. W. Gies, and J. E. Curtin, *J. Vac. Sci. Technol. B* **15**, 2887 (1997).
- ⁹N. R. Tas, J. W. Berenschot, P. Mela, H. V. Jansen, M. Elwenspoek, and A. van den Berg, *Nano Lett.* **2**, 1031 (2002).
- ¹⁰J. Haneveld, H. Jansen, E. Berenschot, N. Tas, and M. Elwenspoek, *J. Micromech. Microeng.* **13**, S62 (2003).
- ¹¹J. Haneveld, E. Berenschot, P. Maury, and H. Jansen, *J. Micromech. Microeng.* **16**, S24 (2006).
- ¹²H. T. Hoang, I. M. Segers-Nolten, J. W. Berenschot, M. J. de Boer, N. R. Tas, J. Haneveld, and M. Elwenspoek, *J. Micromech. Microeng.* **19**, 065017 (2009).
- ¹³J. Huang, M. Juskiewicz, W. H. de Jeu, E. Cerda, T. Emrick, N. Menon, and T. P. Russell, *Science* **317**, 650 (2007).
- ¹⁴D. Vella, J. Bico, A. Boudaoud, B. Roman, and P. M. Reis, *Proc. Natl. Acad. Sci. U.S.A.* **106**, 10901 (2009).
- ¹⁵M.-W. Moon, K.-R. Lee, K. H. Oh, and J. W. Hutchinson, *Acta Mater.* **52**, 3151 (2004).
- ¹⁶E. Cerda, K. Ravi-Chandar, and L. Mahadevan, *Nature (London)* **419**, 579 (2002).
- ¹⁷E. Cerda and L. Mahadevan, *Phys. Rev. Lett.* **90**, 074302 (2003).
- ¹⁸A. I. Fedorchenko, A.-B. Wang, V. I. Mashanov, and H.-H. Cheng, *J. Mech.* **21**, 131 (2005).
- ¹⁹S. Tarasovs and J. Andersons, *Int. J. Solids Struct.* **45**, 593 (2008).
- ²⁰T. Thorsen, S. J. Maerkl, and S. R. Quake, *Science* **298**, 580 (2002).
- ²¹N. Bowden, S. Brittain, A. G. Evans, J. W. Hutchinson, and G. M. Whitesides, *Nature (London)* **393**, 146 (1998).
- ²²W. T. S. Huck, N. Bowden, P. R. Onck, T. Pardoën, J. W. Hutchinson, and G. M. Whitesides, *Langmuir* **16**, 3497 (2000).
- ²³K. Efimenko, M. Rackaitis, E. Manias, A. Vaziri, L. Mahadevan, and J. Genzer, *Nature Mater.* **4**, 293 (2005).
- ²⁴Y. Mei, D. J. Thurmer, F. Cavallo, S. Kiravittaya, and O. G. Schmidt, *Adv. Mater.* **19**, 2124 (2007).
- ²⁵A. Malachias, Y. Mei, R. K. Annabattula, C. Deneke, P. R. Onck, and O. G. Schmidt, *ACS Nano* **2**, 1715 (2008).
- ²⁶S. Edmondson, K. Frieda, J. E. Comrie, P. R. Onck, and W. T. S. Huck, *Adv. Mater.* **18**, 724 (2006).
- ²⁷G. A. Buxton and N. Clarke, *Soft Matter* **2**, 678 (2006).
- ²⁸X. P. Xu and A. Needleman, *Modell. Simul. Mater. Sci. Eng.* **1**, 111 (1993).
- ²⁹F. Bloom and D. Coffin, *Handbook of Thin Plate Buckling and Postbuckling* (Chapman and Hall/CRC, New York, 2001).
- ³⁰See supplementary material at <http://link.aps.org/supplemental/10.1103/PhysRevB.81.224114> for supporting information and a detailed derivation.
- ³¹ABAQUS, *Abaqus V6.7 Documentation*, Dassault systems, Simulia, Rising Sun Mills 166 Valley Street Providence RI 02909–2499 USA (V 6.7).
- ³²L. S. Cheo and E. L. Reiss, *SIAM J. Appl. Math.* **26**, 490 (1974).
- ³³This also causes the numerical procedure to become unstable when a number of these splitting events develop simultaneously. Only for small L_e , the system is able to accommodate the entire strain level of 1.1%, due to the absence of splitting of buckles.
- ³⁴L. Bauer and E. L. Reiss, *J. Soc. Ind. Appl. Math.* **13**, 603 (1965).
- ³⁵G. J. Stroebeel and W. H. Warber, *J. Elast.* **3**, 185 (1973).